pp 1176–1198. © Royal Aeronautical Society 2018
doi: 10.1017/aer.2018.74

Analytical structural behaviour of elastic flapping wings under the actuator effect

H. Zare, Seid H. Pourtakdoust
pourtak@sharif.edu

A. Bighashdel

Center for Research and Development in Space Science and Technology
Sharif University of Technology
Tehran- Iran

ABSTRACT

The effect of inertial forces on the Structural Dynamics (SD) behaviour of Elastic Flapping Wings (EFWs) is investigated. In this regard, an analytical modal-based SD solution of EFW undergoing a prescribed rigid body motion is initially derived. The formulated initial-value problem is solved analytically to study the EFW structural responses, and sensitivity with respect to EFWs' key parameters. As a case study, a rectangular wing undergoing a prescribed sinusoidal motion is simulated. The analytical solution is derived for the first time and helps towards a conceptual understanding of the overall EFW's SD behaviour and its analysis required in their designs. Specifically, the EFW transient and steady response in on-off servo condition is also attended.

Keywords: Elastic flapping wing; structural dynamics; analytical solution; modal approach

Received 4 May 2017; revised 11 March 2018; accepted 25 May 2018; first published online 4 July 2018.

NOMENCLATURE

a_n	normal acceleration of the mass element
A_1, A_2, A_3	motion amplitude parameters
$\mathbf{C}$	damping matrix
$\tilde{\mathbf{C}}$	transformed damping matrix
D	domain
dF_I	the applied inertial force by the mass element
dm	mass element
DOF	Degree-Of-Freedom
E	modulus of elasticity
$\mathbf{F}$	force vector
$\tilde{\mathbf{F}}$	transformed force vector
$\mathbf{F}_I$	inertial force vector
f_d	damping force
f_{ij}	applied forces to the mass element
FEM	Finite Element Method
G	shear modulus
$\mathbf{K}$	stiffness matrix
$\tilde{\mathbf{K}}$	transformed stiffness
m	mass
$\mathbf{M}$	mass matrix
$\tilde{\mathbf{M}}$	transformed mass matrix
N_r	generalised force
P	arbitrary point of domain
P_E	point position after wing deformation
P_R	point position before wing deformation
r	mode number
s	laplace variable
$\boldsymbol{S}_{P_E I}, \boldsymbol{S}_{P_R I}, \boldsymbol{S}_{P_E P_R}$	displacement vectors
t	time
t_{final}	final time of simulation
t_{glide}	gliding time
v_0	initial velocity
w_0	initial displacement
$\mathbf{W}$	displacement vector
z_E	elastic displacement
γ	flapping angle
γ_o	initial angle before gliding phases
γ_{Input}	desired flapping angle
γ_{glide}	gliding angle
γ_{max}	maximum flapping angle
Γ_r	generalised inertial moment
ζ_r	structural damping ratio
ζ_s	control damping ratio
η	vector of generalised coordinate
η_r	generalised coordinate
η_{r0}	initial generalised coordinate

https://doi.org/10.1017/aer.2018.74 Published online by Cambridge University Press

$\dot{\eta}_{r0}$	initial generalised coordinate derivative
ρ	density
$\boldsymbol{\phi}_r$	mode shape vector
$\boldsymbol{\Phi}$	matrix of mode shapes
$\boldsymbol{\Psi}$	non-linear matrix
$\tilde{\boldsymbol{\Psi}}$	transformed non-linear matrix
ω_c	control natural frequency
ω_{dc}	control damped frequency
ω_{dr}	structural damped frequency
ω_f	flapping frequency
ω_r	structural natural frequency

1.0 INTRODUCTION

Flapping Aerial Vehicles (FAVs) have attracted worldwide interest for their possible applications in a wide range of activities, such as monitoring and surveillance. FAVs use flapping wing mechanism to fly, while simultaneously producing thrust and lift. Both bird-like and insect-like flyers utilise flexible flapping wings which have anisotropic flexibilities in chordwise and spanwise directions[1]. Based on their structures, flapping wings undergo moderate to large flexible deformation during flight[2].

The flexibility has a significant effect on the FAVs aerodynamic loading[3-10] which has frequently been validated, experimentally[11-19]. The importance of this phenomenon has led many researches to study the modelling aspects of EFW SD behaviour. Larijani and Delaurier[20], developed a non-linear aeroelastic model for flapping-wing flight based on structural Finite Element Formulation (FEM) and an unsteady aerodynamics approach. Singh and Chopra[21], performed an aeroelastic analysis for hover-capable, bio-inspired flapping wings using unsteady aerodynamics and FEM with plate elements, while the Hamilton's principle was utilised to derive the equations of motion. Gogulapati et al[22] presented a non-linear aeroelastic model for flapping wings undergoing prescribed rigid body motion with moderate to large flexible deformation. Banerjee and Patil[23], employed a Vortex Lattice Method (VLM) to analyse aeroelastics of membrane wings supported by a rigid frame. Kim and Han[24] also suggested a structural dynamic model for flexible wings for application to flapping via an improved modified strip theory, where a modal approach is utilised for structural analysis. Chimakurthi et al[25] used a computational aeroelasticity framework to analyse FAVs. Their structural model comprised of an in-house developed UM/NLABS software that decomposes 3D elasticity equations into cross-sectional and spanwise groups for slender wings using a pressure-based flow-solver algorithm implemented in STREAM[26]. Aono et al[27] presented a numerical framework to simulate rigid and flexible flapping wings. They utilise a Navier-Stokes solver and a flexible multi-body type FEM with triangular facet shell elements to analyse the EFW. Su and Cesnik[28] analysed non-linear aeroelasticity of a FAV. They incorporated two types of unsteady aerodynamic formulations, where geometrically non-linear deformations were modelled via non-linear strain-based beam formulation. Pourtakdoust and Karimain Aliabadi[29] developed an aeroelastic model of a typical EFW to evaluate propulsive efficiency. They employed the Euler–Bernoulli torsion beam with quasi-steady aerodynamic model to study the effect of mass, inertia, elastic properties as well as the flapping amplitude and frequency of the FMAV. De Rosis et al[30] conducted an aeroelastic study of flexible flapping wings using a coupled lattice

https://doi.org/10.1017/aer.2018.74 Published online by Cambridge University Press

Boltzmann-finite element approach, where fluid-structure interface conditions were handled using an immersed boundary method. Lakshminarayan and Farhat[31] used a recently developed ALE-embedded method to perform high-fidelity aeroelastic analysis of extremely flexible flapping wings. Nogar et al[32] developed a computationally efficient approximate aeroelastic model suitable for control applications in which aerodynamic loads are calculated via a quasi-static model and the structural model is generated using an implicit condensation approach. Ha et al[33] presented a computational approach to investigate fluid structural coupling of EFWs. They used a geometrically exact beam model for the structural analysis and a preconditioned Navier-Stokes solver for aerodynamic analysis. Their study revealed that a limited degree of flexibility is beneficial, while high-flexibility leads to thrust deterioration. Djojodihardjo[34] recently conducted a comprehensive study on aerodynamics, aeroelasticity and flight dynamics of birdlike flapping wing ornithopter in forward flight. Using an unsteady aerodynamic approach, author-incorporated viscous effects and leading-edge suction together with a simplified two-dimensional beam theory to gain some insight over the effect of aeroelasticity via low-cost methods.

With respect to the existence of several loads in flapping flight including aerodynamics, gravitation, structure and inertia, some researchers have compared the effect of these forces in flexibility, implicitly or explicitly. For instance, Combes and Daniel[11] experimentally investigated the contributions of aerodynamic and inertial elastic forces for an specific wing. They compared wing-bending results for normal air versus helium and showed that contribution of fluid-dynamic forces to wing deformations is significantly reduced. This relatively huge reduction in air density produced only slight changes in the pattern of the wing deformations, suggesting that fluid-dynamic forces have minimal effect on the wing bending. However, they emphasised that this claim is reliable for certain combinations of wing stiffness, wing motions, and fluid density[35]. This conclusion proposes that in some conditions, the inertial forces effect in EFW behaviour is of premier importance. In this regard, some researchers focused on inertial forces. Barut et al[36] utilised FEM concepts in conjunction with non-linear theory of elasticity and rigid-body dynamics to investigate the effect of prescribed dynamic motion and flexibility on the EFW deformation in absence of aerodynamic loads. Their study included the effect of inertial forces due to centrifugal and Coriolis accelerations caused by wing flapping and pitching motions as well as the stress-induced forces due to considerable stretching and bending deformations occurring in the wing. Wilson and Wereley[37] experimentally investigated the performance of an insect-like EFW and quantified the lifting force in hover condition. They used an experimental test-stand to flap the wings with 1 and 2 degrees of freedom and measured the wing loadings. Additionally, to identify the non-aerodynamic forces, they performed their tests in a vacuum chamber as well. Yeo et al[38] also used a vacuum chamber to measure non-aerodynamic forces of a EFW.

The current study is focused on derivation of an analytical solution for SDE of EFW that has not yet been attempted in the literature. Due to importance of inertial forces[11] for bird-like structures, only the inertial forces are considered. Further, the effect of servo dynamics for resonance behaviour is also considered. For this purpose, the SDE governing an EFW is derived using the modal approach that is widely used for elasticity analysis of various flying vehicles including EFWs[24,39], missiles[40,41], aircrafts[42] and airships[43]. In all latter studies, deflections are expanded in terms of the normal structural modes where the final governing equations are derived using the orthogonality conditions. In this scheme, the EFW natural frequencies and mode shapes are obtained via FEM analysis. To develop an analytical solution, it is assumed that the structure responses lie within the linear range. This is valid

https://doi.org/10.1017/aer.2018.74 Published online by Cambridge University Press

for a low flapping frequency range that in turn yields a low flapping-to-structure frequency ratio. Considering this assumption, the coupling effects between various structural modes can be ignored and the governing SD equations become linear and uncoupled. The resulting analytical solution enables one to assess and evaluate the coupling between the imposed forcing, structure and the servo dynamics, thus providing a conceptual understanding for the overall EFW SD behaviour in the presence of inertial forces plus the servo dynamics effects.

The remainder of this paper is organised as follows: Section 2.0 describes the formulation of the SDE, inertial forces and servo motor dynamics. Sections 3.0 and 4.0 are devoted to the development of the analytical solution of rigid and elastic wing motion. Section 5.0 delivers the verification and simulation results for a typical EFW under various loading scenarios, followed by conclusions in Section 6.0.

2.0 FORMULATION

2.1 Structure model

Accurate prediction of large amplitude structural deformations is feasible via non-linear finite element models. However, representation of complex system equations of motion in finite element nodal space requires large degrees of freedom and computational cost that is impractical for design applications[44]. The governing structural equations of motion for a multiple Degree-Of-Freedom (DOF), geometrically non-linear system with viscous damping can be written as[45]:

$$\mathbf{M}\ddot{\mathbf{W}}(t) + \mathbf{C}\dot{\mathbf{W}}(t) + \mathbf{K}\mathbf{W}(t) + \mathbf{\Psi}(\mathbf{W}(t)) = \mathbf{F}(t) \quad \ldots(1)$$

where $\mathbf{M}$, $\mathbf{C}$ and $\mathbf{K}$ are the mass, damping, and stiffness matrices, respectively; $\mathbf{W}$ is the displacement vector and $\mathbf{F}$ represents the force excitation vector. The non-linear forcing term $\mathbf{\Psi}(\mathbf{W}(t))$ is a non-linear vector function of $\mathbf{W}$.

An alternative solution approach of the above equation is via transformation to a reduced basis modal coordinate system that dramatically reduces the number of DOFs[46]. The generalised coordinate transformation approach is implemented to obtain a set of coupled modal equations, with reduced DOF:

$$\mathbf{W} = \mathbf{\Phi}\eta, \quad \ldots(2)$$

where $\boldsymbol{\eta}$ and $\mathbf{\Phi}$ are time-dependent vectors of generalised coordinates and a subset of linear eigenvectors (assumed mode shapes vectors), respectively. Via the above transformation, the modal equation results:

$$\tilde{\mathbf{M}}\ddot{\boldsymbol{\eta}} + \tilde{\mathbf{C}}\dot{\boldsymbol{\eta}} + \tilde{\mathbf{K}}\boldsymbol{\eta} + \tilde{\mathbf{\Psi}}(\boldsymbol{\eta}) = \tilde{\mathbf{F}}, \quad \ldots(3)$$

where

$$\tilde{\mathbf{M}} = \mathbf{\Phi}^{\mathbf{T}}\mathbf{M}\mathbf{\Phi} = [I] \quad \ldots(4)$$

$$\tilde{\mathbf{C}} = \mathbf{\Phi}^{T}\mathbf{C}\mathbf{\Phi} = [2\zeta_r\omega_r] \quad \ldots(5)$$

$$\tilde{\mathbf{K}} = \mathbf{\Phi}^{T}\mathbf{K}\mathbf{\Phi} = \left[\omega_r^2\right] \quad \ldots(6)$$

https://doi.org/10.1017/aer.2018.74 Published online by Cambridge University Press

$$\tilde{\boldsymbol{\Psi}}(\boldsymbol{\eta}) = \boldsymbol{\Phi}^{\mathrm{T}}\boldsymbol{\Psi}(\boldsymbol{\eta}) \quad \ldots(7)$$

$$\tilde{\mathbf{F}} = \boldsymbol{\Phi}^{\mathrm{T}}\mathbf{F} = [N_r], \quad \ldots(8)$$

where ω_r, ζ_r and N_r are the undamped natural frequencies, damping coefficient and generalised forces, respectively, for the r^{th} mode. As seen in Equation (3), $\tilde{\boldsymbol{\Psi}}(\boldsymbol{\eta})$ brings about the non-linearity and as well as coupling in to the system of equations. However, in absence of large structural displacement, it can be ignored and thus resulting in an uncoupled, linear system of equations as follows:

$$\ddot{\eta}_r(t) + 2\zeta_r\omega_r\dot{\eta}_r(t) + \omega_r^2\eta_r(t) = N_r(t); \quad r = 1, 2, \ldots \quad \ldots(9)$$

in which the generalised forces are defined as:

$$N_r(t) = \int_D \phi_r(P) F(P,t)\, dD(P), \quad r = 1, 2, \ldots \quad \ldots(10)$$

where P is an arbitrary point within the domain D.

Equation (9) is subject to the initial generalised displacements and velocities, given below:

$$\eta_r(0) = \int_D m(P)\phi_r(P) w_0(P)\, dD(P), \quad r = 1, 2, \ldots \quad \ldots(11)$$

$$\dot{\eta}_r(0) = \int_D m(P)\phi_r(P) v_0(P)\, dD(P), \quad r = 1, 2, \ldots, \quad \ldots(12)$$

where w_0 and v_0 are initial displacement and velocity, respectively.

2.2 Inertial force modelling

Due to accelerated motion of the EFW, centrifugal and normal forces are applied to each element. Considering the inherent in-plane tensile strength of the EFW, centrifugal forces are neglected. This is justified as natural frequencies of in-plane modes are normally a few orders of magnitude higher than the natural frequencies of the out-plane ones. Thus, omission of the apparent centrifugal forces is not due to their smaller values, but because of their small effects on structural displacements.

According to Fig. 1, the summation of normal inertial forces applied to an element due to angular acceleration is:

$$\sum_{i,j} \mathbf{F}_{z_{ij}} = a_n dm = y[-\ddot{\gamma}(t)]\, dm, \quad \ldots(13)$$

where $\mathbf{F}_{ij}$ is the applied force caused by neighboring elements, a_n and y are the linear acceleration and position of the mass element dm, respectively, and $\ddot{\gamma}(t)$ is the angular acceleration of the EFW. Please note that the minus sign in Equation (13) is due to the reference definition of the γ. Thus, according to the Newton's third law of reaction, the applied inertial force from this element to EFW will be:

$$dF_I = -y[-\ddot{\gamma}(t)]\, dm = y\ddot{\gamma}(t)\, dm \quad \ldots(14)$$

https://doi.org/10.1017/aer.2018.74 Published online by Cambridge University Press

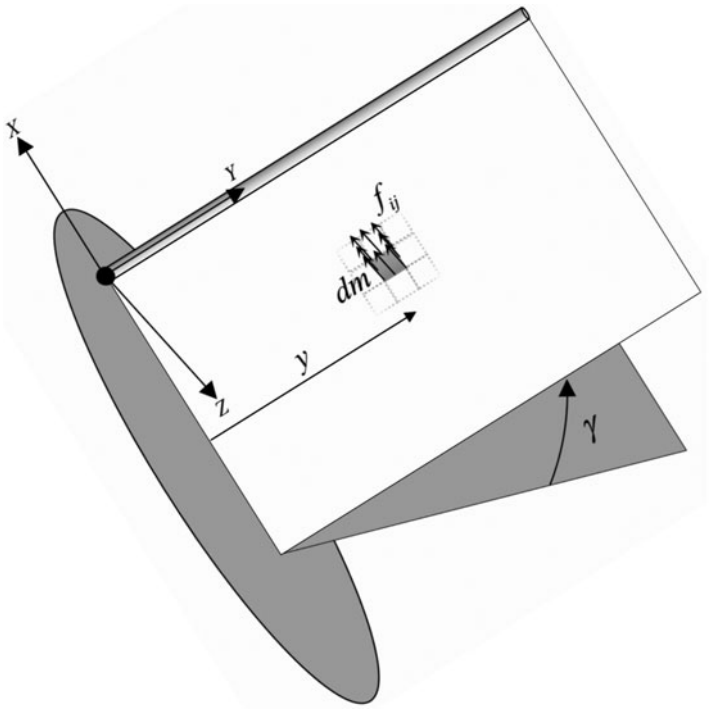

Figure 1. Overall scheme of the inertial forces applied to an element.

Referring to Equation (14), one we can define generalised forces as follows:

$$N_r(t) = \int_D \phi_r dF_I = \int_A \phi_r y \ddot{\gamma}(t)\, dm = \sum_{i,j} \phi_{r_{i,j}} y_{i,j} \ddot{\gamma}(t)\, dm_{i,j} = \ddot{\gamma}(t)\, \mathbf{\Gamma}_r, \quad \ldots(15)$$

where

$$\mathbf{\Gamma}_r = \sum_{i,j} \mathbf{f}_{r_{i,j}} y_{i,j} dm_{i,j} \quad \ldots(16)$$

It is realized that, Γ_r turns out as a structural property that depends on the structure mass distribution and is motion independent. In this sense, it can be referred to as 'Generalised Inertial Moment' or GIM.

2.3 Servo motor dynamics

The objective of the servo systems is to control the position of a mechanical system in accordance with a prescribed position. The difference between the input command angular position and the output angular position is the error signal[47]. To model the servo actuator effects on the dynamic response of the EFW, a second order servo dynamics is considered (see Equation (17)) whose transfer function is suggested[47], with adjustable parameters ζ_c

https://doi.org/10.1017/aer.2018.74 Published online by Cambridge University Press

and ω_c defined in the nomenclature.

$$G(s) = \frac{\omega_c^2}{s^2 + 2\zeta_c\omega_c s + \omega_c^2} \quad \ldots(17)$$

3.0 ANALYTICAL SOLUTION OF RIGID WING MOTION

In analogy with actual flying EFWs like a bird, it is possible for the flapping motion to stop in a gliding phase of flight. Accordingly, the desired flapping motion can be broken in to a sinusoidal part followed by a command to stop the flapping at a static value. In this respect, the following subsection presents the analytic results of such commands as implemented via a servo actuator.

3.1 Sinusoidal flapping command

Since a part of the EFW motion is sinusoidal, this section will present an analytical solution for the controller output (Equation (17)). As already discussed in Section 2.0, considering a second order transfer function for the controller, will yield,

$$\frac{\gamma}{\gamma_{\text{Input}}}(s) = \frac{\omega_c^2}{s^2 + 2\zeta_c\omega_c s + \omega_c^2}, \quad \ldots(18)$$

where

$$\gamma_{\text{Input}}(t) = \gamma_{\max}\sin\left(\omega_f t\right) \quad \ldots(19)$$

Subsequently, the controller output is determined via Laplace transformations that results in:

$$\gamma(s) = \frac{\gamma}{\gamma_{\text{Input}}}(s)\,\gamma_{\text{Input}}(s) = \frac{\gamma_{\max}\omega_f\omega_c^2}{\left(s^2 + 2\zeta_c\omega_c s + \omega_c^2\right)\left(s^2 + \omega_f^{22}\right)} \quad \ldots(20)$$

$$\gamma(t) = e^{-\zeta_c\omega_c t}A_{22}\sin\left(\omega_{\text{dc}}t + \phi_{22}\right) + A_{11}\sin\left(\omega_f t + \phi_{11}\right) \quad \ldots(21)$$

with the following parameters that are intelligently defined for sensitivity analysis of the EFW response,

$$\omega_{\text{dc}} = \omega_c\sqrt{1 - \zeta_c^2}, \quad \ldots(22)$$

$$A_{21} = \frac{\gamma_{\max}\frac{\omega_f}{\omega_c}}{\left(\frac{\omega_f}{\omega_c}\right)^4 - 2\left(1 - 2\zeta_c^2\right)\left(\frac{\omega_f}{\omega_c}\right)^2 + 1}, \quad \ldots(23)$$

$$A_{22} = A_{21}\sqrt{\left(\frac{1}{\sqrt{1-\zeta_c^2}}\left[\left(\frac{\omega_f}{\omega_c}\right)^2 - \left(1 - 2\zeta_c^2\right)\right]\right)^2 + (2\zeta_c)^2}, \quad \ldots(24)$$

https://doi.org/10.1017/aer.2018.74 Published online by Cambridge University Press

$$A_{11} = A_{21}\sqrt{\left(\left(\frac{\omega_f}{\omega_c}\right)^{-1} - \frac{\omega_f}{\omega_c}\right)^2 + (2\zeta_c)^2}, \quad \ldots(25)$$

$$\phi_{22} = \tan^{-1}\left(\frac{2\zeta_c\sqrt{1-\zeta_c^2}}{\left(\frac{\omega_f}{\omega_c}\right)^2 - \left(1-2\zeta_c^2\right)}\right), \quad \ldots(26)$$

$$\phi_{11} = \tan^{-1}\left(-\frac{2\zeta_c\frac{\omega_f}{\omega_c}}{1-\left(\frac{\omega_f}{\omega_c}\right)^2}\right) \quad \ldots(27)$$

Noting Equation (21), the controller response (to sinusoidal input) contains a transient fading part plus a time varying portion that can be regarded as a steady forcing on the EFW that is obtained as follows:

$$\begin{aligned}\lim_{t\to\infty}\gamma(t) &= \lim_{t\to\infty}\left[e^{-\zeta_c\omega_c t}A_{22}\sin(\omega_{dc}t+\phi_{22}) + A_{11}\sin\left(\omega_f t+\phi_{11}\right)\right]\\ &= A_{11}\sin\left(\omega_f t+\phi_{11}\right)\\ &= \gamma_{max}\frac{\frac{\omega_f}{\omega_c}\sqrt{\left(\left(\frac{\omega_f}{\omega_c}\right)^{-1}-\frac{\omega_f}{\omega_c}\right)^2+(2\zeta_c)^2}}{\left(\frac{\omega_f}{\omega_c}\right)^4-2\left(1-2\zeta_c{}^2\right)\left(\frac{\omega_f}{\omega_c}\right)^2+1}\sin\left(\omega_f t+\phi_{11}\right)\end{aligned} \quad \ldots(28)$$

Comparing the above analytic controller output with the sinusoidal input (Equation (19)), one can realize the effect of servo dynamics on both amplitude and phase shift of the sinusoidal forcing motion. In other words, for a very fast actuator with a high operating frequency sufficiently greater than EFW flapping frequency, the flapping motion will be close to the commanded value.

$$\lim_{t\to\infty,\ \frac{\omega_f}{\omega_c}\to 0}\gamma(t) = \gamma_{max}\sin\left(\omega_f t\right) \quad \ldots(29)$$

3.2 Stopping command

In this case, it is assumed that the EFW flapping is suddenly commanded to perform a stopping manoeuver towards a fixed flapping angle at t_i, such that:

$$\gamma_{Input} = \Delta\gamma_{glide}; \quad \Delta\gamma_{glide} = \gamma_{Stop} - \gamma(t_i), \quad \ldots(30)$$

where $\gamma(t_i)$ and γ_{Stop} are the current and final flapping angles of the EFW for a final glide operation, respectively. Again, via Laplace transformation, one can show the actual commanded result due to the servo dynamic to be as follows:

$$\begin{aligned}\gamma(s) &= \frac{\gamma}{\gamma_{Stop}}(s)\,\gamma_{Stop}(s)\\ &= \frac{\Delta\gamma_{glide}\omega_c^2}{s\left(s^2+2\zeta_c\omega_c s+\omega_c^2\right)},\end{aligned} \quad \ldots(31)$$

$$\gamma(t) = \gamma_{Stop} - e^{-\zeta_c\omega_c t}B_{11}\sin\left(\omega_{dc}t+\psi_{11}\right), \quad \ldots(32)$$

https://doi.org/10.1017/aer.2018.74 Published online by Cambridge University Press

where

$$B_{11} = \frac{\Delta\gamma_{\text{glide}}}{\sqrt{1-\zeta_c^2}}; \quad \psi_{11} = \tan^{-1}\left(\frac{\sqrt{1-\zeta_c^2}}{\zeta_c}\right) \qquad \ldots (33)$$

Additionally, similar to Section 3.1, one can observe that limiting desired value is eventually reached after some elapsed time.

$$\lim_{t\to\infty}\gamma(t) = \gamma_{\text{Stop}} \qquad \ldots (34)$$

It is realized from Equations (32) and (34) that the controller dynamics does not have any effect on the final steady result and the actuator will finally place the EFW at the desired flapping position. The resulting graphical summary of the above cases are shown in Fig. 4 as a part of the simulation scenario presented in Section 5.0.

4.0 ANALYTICAL SOLUTION OF EFW

In this section, the analytical solution for the structural behaviour of the EFW is presented. The analytical solution is developed in two parts that includes response to a pure flapping command as well as the EFW response to a flap angle command.

4.1 Sinusoidal flapping response

As a requirement for the solution of the governing structural equations, Equations (9) and (15), $\ddot{\gamma}(t)$ is required to calculate the generalised forces. In this respect, one can obtain the flapping angular acceleration via Equation (21), to be:

$$\ddot{\gamma}(t) = e^{-\zeta_c\omega_c t}\left[\hat{A}_{22}\sin\left(\omega_{\text{dc}}t + \hat{\phi}_{22}\right)\right] + \hat{A}_{11}\sin\left(\omega_f t + \phi_{11}\right), \qquad \ldots (35)$$

where

$$\hat{A}_{22} = -A_{22}\omega_c^2; \;\; \hat{A}_{11} = -A_{11}\omega_f^2; \quad \hat{\phi}_{22} = \phi_{22} + \tan^{-1}\left(\frac{2\zeta_c\sqrt{1-\zeta_c^2}}{1-2\zeta_c^2}\right) \qquad \ldots (36)$$

Substituting Equation (35) in Equation (15) and Equation (9) yields the desired Ordinary Differential Equation (ODE) for dynamic behaviour of the EFW under sinusoidal actuation.

$$\begin{aligned}&\ddot{\eta}_r(t) + 2\zeta_r\omega_r\dot{\eta}_r(t) + \omega_r^2\eta_r(t) = \hat{A}_{22}\mathbf{\Gamma}_r e^{-\zeta_c\omega_c t}\sin\left(\omega_{\text{dc}}t + \hat{\phi}_{22}\right) + \mathbf{\Gamma}_r\hat{A}_{11}\sin\left(\omega_f t + \phi_{11}\right)\\ &\quad \eta_r(0) = \eta_{r0}; \quad \dot{\eta}_r(0) = \dot{\eta}_{r0}\end{aligned} \qquad \ldots (37)$$

The analytical solution of this ODE is determined using the specified initial conditions.

$$\begin{aligned}\eta_r(t) = {} & A_1\sin\left(\omega_f t + \phi_1\right) + e^{-\zeta_c\omega_c t}A_2\sin\left(\omega_{\text{dc}}t + \phi_2\right)\\ & + e^{-\zeta_r\omega_r t}A_3\sin\left(\omega_{dr}t + \phi_3\right), \quad r = 1, 2, \ldots,\end{aligned} \qquad \ldots (38)$$

https://doi.org/10.1017/aer.2018.74 Published online by Cambridge University Press

where

$$\omega_{dr} = \omega_r\sqrt{1-\zeta_r^2}, \quad \ldots(39)$$

$$A_3 = \frac{\eta_{r0} - A_2\sin(\phi_2) - A_1\sin(\phi_1)}{\sin(\phi_3)}, \quad \ldots(40)$$

$$\phi_3 = \tan^{-1}\left\{\frac{\frac{\omega_r}{\omega_c}\sqrt{1-\zeta_r^2}[\eta_{r0}-A_2\sin(\phi_2)-A_1\sin(\phi_1)]}{\frac{\eta_{r0}}{\omega_c}-A_1\frac{\omega_f}{\omega_c}\cos(\phi_1)+\zeta_c A_2\sin(\phi_2)-\sqrt{1-\zeta_c^2}A_2\cos(\phi_2)+\zeta_r\frac{\omega_r}{\omega_c}[\eta_{r0}-A_2\sin(\phi_2)-A_1\sin(\phi_1)]}\right\}, \quad \ldots(41)$$

$$A_2 = -\frac{\Gamma_r A_{22}}{\sqrt{\left[\left(\frac{\omega_r}{\omega_c}\right)^2-(1-2\zeta_c^2)-2\xi_r\zeta_c\left(\frac{\omega_r}{\omega_c}\right)\right]^2+\left[2\zeta_r\left(\frac{\omega_r}{\omega_c}\right)\sqrt{1-\zeta_c^2}-2\zeta_c\sqrt{1-\zeta_c^2}\right]^2}}, \quad \ldots(42)$$

$$A_1 = \frac{-\Gamma_r\left(\frac{\omega_f}{\omega_r}\right)^2 A_{11}}{\sqrt{\left(1-\left(\frac{\omega_f}{\omega_r}\right)^2\right)^2+\left(2\zeta_r\left(\frac{\omega_f}{\omega_r}\right)\right)^2}}, \quad \ldots(43)$$

$$\phi_2 = \tan^{-1}\left(\frac{2\zeta_c(1-\zeta_c^2)}{\left(\frac{\omega_f}{\omega_c}\right)^2-(1-2\zeta_c^2)}\right)+\tan^{-1}\left(\frac{2\zeta_c\sqrt{1-\zeta_c^2}}{1-2\zeta_c^2}\right)-\tan^{-1}\left(\frac{2\zeta_r\frac{\omega_r}{\omega_c}\sqrt{1-\zeta_c^2}-2\zeta_c\sqrt{1-\zeta_c^2}}{\left(\frac{\omega_r}{\omega_c}\right)^2-2\zeta_r\zeta_c\frac{\omega_r}{\omega_c}-(1-2\zeta_c^2)}\right), \quad \ldots(44)$$

$$\phi_1 = \tan^{-1}\left(-\frac{2\zeta_c\frac{\omega_f}{\omega_c}}{1-\left(\frac{\omega_f}{\omega_c}\right)^2}\right)-\tan^{-1}\left(\frac{2\xi_r\frac{\omega_f}{\omega_r}}{1-\left(\frac{\omega_f}{\omega_r}\right)^2}\right) \quad \ldots(45)$$

The resulting analytical solution (Equations (38) to (45)) indicates that larger natural frequencies of the structural mode shapes tend to have no significant effect on the EFW dynamic behaviour, as shown below:

$$\lim_{\omega_r\to\infty}\eta_r(t) = 0 \quad \ldots(46)$$

In addition, it is also seen that at Structure-Actuator Frequency Ratio (SAFR) close to one, i.e. $\omega_r/\omega_c \to 1$, existence of the actuation damping, ζ_c effectively bounds A_2 (Equation (42)) that in turn prevents the second term of the EFW dynamic response (Equation (38)) from growing. To check the conditions for other resonance behaviours, other coefficients will also be examined. In this respect, when there is insignificant or zero structural damping, $\zeta_r \to 0$, A_1 and consequently A_3 tend towards infinity at Structure-Flapping Frequency Ratio (SFFR) close to one i.e. $\omega_f/\omega_r \to 1$. Figure 2 shows the variation of A_1 for two different values of ζ_r as a function of SAFR and SFFR. According to this figure, it is seen that A_1 achieves its pick value for resonance conditions of both frequency ratios i.e. $\omega_f/\omega_r \to 1$ and $\omega_r/\omega_c \to 1$. Finally, Fig. 3 shows the variation of A_1 at resonance conditions as a function of the EFW structural damping, ζ_r.

https://doi.org/10.1017/aer.2018.74 Published online by Cambridge University Press

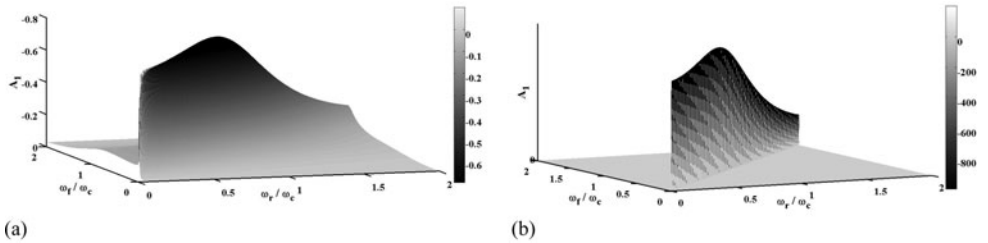

Figure 2. The variation of A_1 values versus frequency ratios at (a) $\zeta_r = 0.07$ and (b) $\zeta_r = 0.00001$.

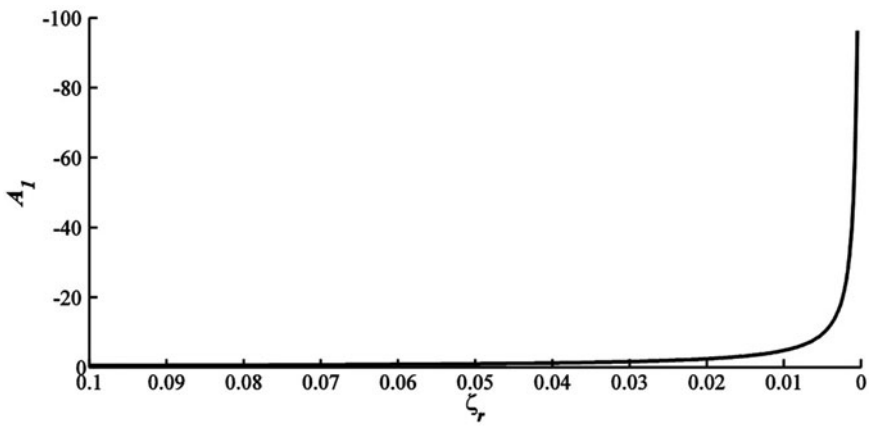

Figure 3. The variation of A_1 values versus structural damping ratio at $\omega_r/\omega_c = \omega_f/\omega_c = 1$.

4.2 Response to flap angle (glide) command

In analogy with the sinusoidal forcing discussed in Section 4.1, flapping acceleration actuator output is again required to calculate generalised forces. Using Equation (32), it can be shown that:

$$\ddot{\gamma}(t) = \hat{B}_{11} e^{-\zeta_c \omega_c t} \sin\left(\omega_{dc} t + \hat{\psi}_{11}\right), \qquad \ldots (47)$$

where

$$\hat{B}_{11} = B_{11}\omega_c^2; \quad \hat{\psi}_{11} = \psi_{11} + \tan^{-1}\left(\frac{2\zeta_c\sqrt{1-\zeta_c^2}}{1-2\zeta_c^2}\right) \qquad \ldots (48)$$

Substituting Equation (47) in Equation (15) and next in Equation (9), the ODE governing EFW structural dynamic response as well as its solution are analytically computed.

$$\ddot{\eta}_r(t) + 2\zeta_r\omega_r\dot{\eta}_r(t) + \omega_r^2\eta_r(t) = \Gamma_r\hat{B}_{11}e^{-\zeta_c\omega_c t}\sin\left(\omega_{dc}t + \hat{\psi}_{11}\right);$$
$$\eta_r(0) = \eta_{r0}; \quad \dot{\eta}_r(0) = \dot{\eta}_{r0}, \qquad \ldots (49)$$

https://doi.org/10.1017/aer.2018.74 Published online by Cambridge University Press

$$\eta_r(t) = e^{-\zeta_r \omega_r t} B_2 \sin(\omega_{dr} t + \psi_2) + B_1 e^{-\zeta_c \omega_c t} \sin(\omega_{\mathrm{dc}} t + \psi_1), \quad r = 1, 2, \ldots, \qquad \ldots (50)$$

where

$$\psi_2 = \tan^{-1}\left\{ \frac{\frac{\omega_r}{\omega_c}\sqrt{1-\zeta_r^2}\,(\eta_{r0} - B_1 \sin(\psi_1))}{\frac{\dot{\eta}_{r0}}{\omega_c} - B_1\sqrt{1-\zeta_c^2}\cos(\psi_1) + \zeta_c B_1 \sin(\psi_1) + \zeta_r \frac{\omega_r}{\omega_c}(\eta_{r0} - B_1 \sin(\psi_1))} \right\}, \qquad \ldots (51)$$

$$B_2 = \frac{\eta_{r0} - B_1 \sin(\psi_1)}{\sin(\psi_2)}, \qquad \ldots (52)$$

$$B_1 = \frac{\frac{\Gamma_r \gamma_{\mathrm{glide}}}{\sqrt{1-\zeta_c^2}}}{\sqrt{\left[2\left(\frac{\omega_r}{\omega_c}\right)\zeta_r\sqrt{1-\zeta_c^2} - 2\zeta_c\sqrt{1-\zeta_c^2}\right]^2 + \left[\left(\frac{\omega_r}{\omega_c}\right)^2 - (1-2\zeta_c^2) - 2\left(\frac{\omega_r}{\omega_c}\right)\zeta_r\zeta_c\right]^2}} \qquad \ldots (53)$$

$$\psi_1 = \tan^{-1}\left(\frac{\sqrt{1-\zeta_c^2}}{\zeta_c}\right) + \tan^{-1}\left(\frac{2\zeta_c\sqrt{1-\zeta_c^2}}{1-2\zeta_c^2}\right) - \tan^{-1}\left(\frac{2\left(\frac{\omega_r}{\omega_c}\right)\zeta_r\sqrt{1-\zeta_c^2} - 2\zeta_c\sqrt{1-\zeta_c^2}}{\left(\frac{\omega_r}{\omega_c}\right)^2 - (1-2\zeta_c^2) - 2\left(\frac{\omega_r}{\omega_c}\right)\zeta_r\zeta_c}\right) \qquad \ldots (54)$$

The result indicates that higher structural modes have insignificant effect on the final static position of the EFW, pending higher modes are not initially excited, or in other words:

$$\lim_{\omega_r \to \infty} \eta_r(t) = 0 \qquad \ldots (55)$$

5.0 CASE STUDY

To better understand the EFW dynamic behaviour subsequent to commanded flapping, a case study is performed in this section where the commanded flapping consists of two parts whose analytical solutions have already been developed. It needs to be mentioned that the EFW natural frequencies and mode shapes are required for dynamic response analysis and calculated via FEM.

5.1 Flapping scenario

To analyse the EFW structural response, a flapping scenario is considered where the actuator initially commands a sinusoidal behaviour (from rest) to be stopped at a certain glide angle. The commanded flapping angle as well as the corresponding servo output are shown in Fig. 4. Subsequently, the EFW corresponding analytical solutions (Equations (38) and (50)) are determined based on the following initial conditions:

$$\begin{cases} \eta_{r_{\mathrm{phase\ I}}}(t=0) = 0 \\ \dot{\eta}_{r_{\mathrm{phase\ I}}}(t=0) = 0 \end{cases}, \qquad \ldots (56)$$

$$\begin{cases} \eta_{r_{\mathrm{phase\ II}}}\left(t = t_{\mathrm{glide}}\right) = \eta_{r_{\mathrm{phase\ I}}}\left(t = t_{\mathrm{glide}}\right) \\ \dot{\eta}_{r_{\mathrm{phase\ II}}}\left(t = t_{\mathrm{glide}}\right) = \dot{\eta}_{r_{\mathrm{phase\ I}}}\left(t = t_{\mathrm{glide}}\right) \end{cases} \qquad \ldots (57)$$

https://doi.org/10.1017/aer.2018.74 Published online by Cambridge University Press

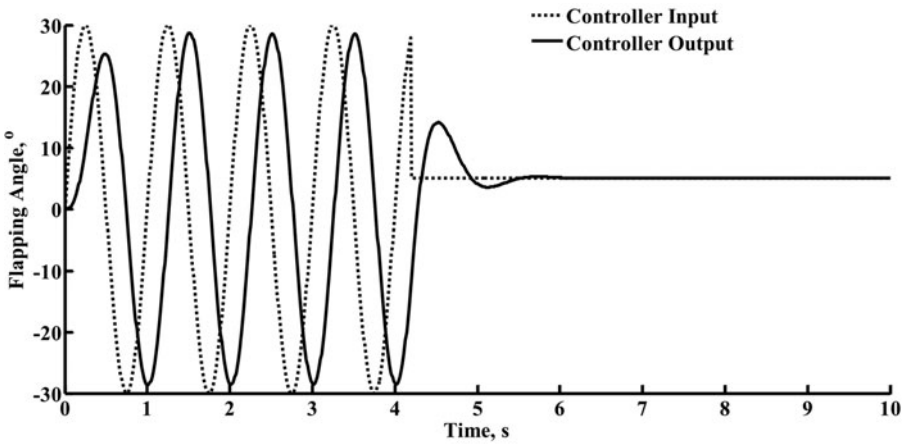

Figure 4. Flapping angle, influenced by the controller dynamics.

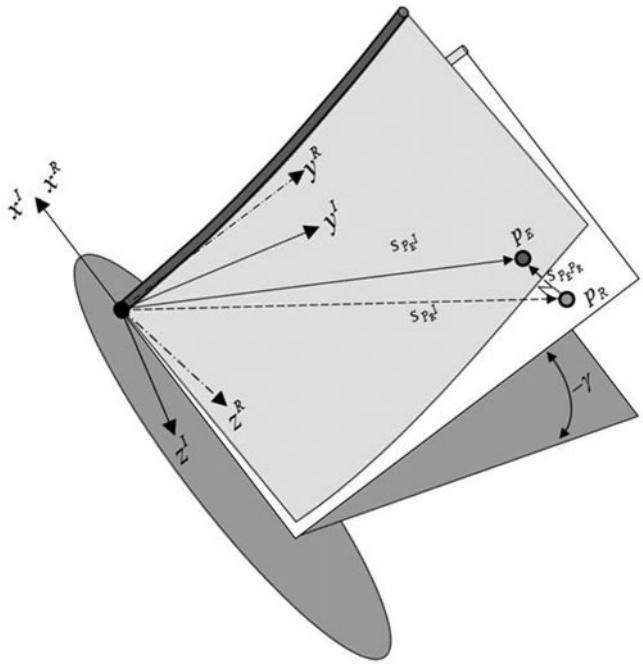

Figure 5. Flapping wing coordinates systems definition.

5.2 Simulation considerations

In this study, only the right wing is modelled and simulated, while the EFW body is considered motionless and fixed to an Inertial Coordinate System (ICS). Therefore, one can specify the EFW rigid motion via a single flapping angle with respect to the ICS. Accordingly, EFW elements will experience a vibrating motion in addition to the aforementioned prescribed rigid body motion, as shown in Fig. 5. As a result, the total inertial position of EFW elements can be

https://doi.org/10.1017/aer.2018.74 Published online by Cambridge University Press

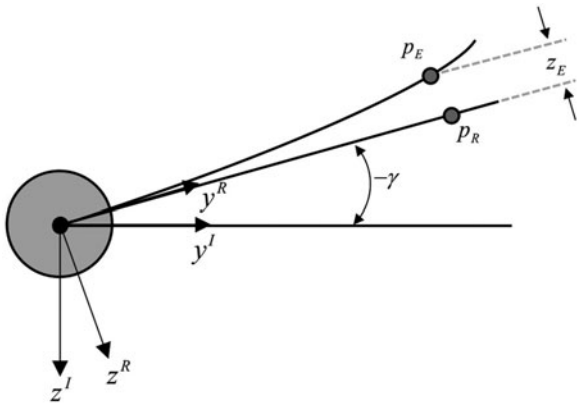

Figure 6. Rear view of the wing in flapping cycle.

computed via superposition of its rotational position plus an elastic deformation emanating from the EFW analytical solutions presented. Additionally, the origin of the ICS is taken at the EFW hinge located at the wing-root leading-edge point, where x^I points forward, z^I points downward within the EFW plane of symmetry and y^I axis is perpendicular to the previous directions to form a right-handed orthogonal system (see Fig. 5). Moreover, a rigid body coordinate system is defined that shows the EFW elements rigid motion via the flapping angleγ whose transformation matrix is given below:

$$[T]^{IR} = \begin{bmatrix} 1 & 0 & 0 \\ 0 & \cos(-\gamma) & \sin(-\gamma) \\ 0 & -\sin(-\gamma) & \cos(-\gamma) \end{bmatrix} \quad \ldots(58)$$

Finally, instantaneous position of any point P_E within the deformed EFW with respect to ICS will be:

$$\boldsymbol{s}_{P_E I} = \boldsymbol{s}_{P_E P_R} + \boldsymbol{s}_{P_R I}, \quad \ldots(59)$$

$$\left[\boldsymbol{s}_{P_E I}\right]^I = \left[\boldsymbol{s}_{P_E P_R}\right]^I + \left[\boldsymbol{s}_{P_R I}\right]^I = [T]^{IR}\left[\boldsymbol{s}_{P_E P_R}\right]^R + [T]^{IR}\left[\boldsymbol{s}_{P_R I}\right]^R \quad \ldots(60)$$

where

$$\left[\boldsymbol{s}_{P_R I}\right]^R = \begin{bmatrix} x^R \\ y^R \\ z^R \end{bmatrix} \; ; \quad \left[\boldsymbol{s}_{P_E P_R}\right]^R = \begin{bmatrix} 0 \\ 0 \\ z^E \end{bmatrix} \; ; \; z^E = \sum_r \eta_r(t)\,\phi_r(P) \quad \ldots(61)$$

The subscript I, R and E are indicative of ICS, rigid EFW local body coordinate system and the elastic local deformation of a typical point on R, respectively. Finally, one can obtain the coordinates of any arbitrary point, P_E with respect to the ICS as, (see Fig. 6).

$$\begin{bmatrix} x^I \\ y^I \\ z^I \end{bmatrix} = \begin{bmatrix} 1 & 0 & 0 \\ 0 & \cos(-\gamma) & \sin(-\gamma) \\ 0 & -\sin(-\gamma) & \cos(-\gamma) \end{bmatrix} \begin{bmatrix} x^R \\ y^R \\ z^E \end{bmatrix} = \begin{bmatrix} x^R \\ y^R\cos(\gamma) - z^E\sin(\gamma) \\ y^R\sin(\gamma) + z^E\cos(\gamma) \end{bmatrix} \quad \ldots(62)$$

https://doi.org/10.1017/aer.2018.74 Published online by Cambridge University Press

Table 1
Natural frequencies of first 10 structural modes

Mode Number	Natural frequency (Hz)
1	2.56
2	6.81
3	16.57
4	27.11
5	44.33
6	57.50
7	59.24
8	68.65
9	71.97
10	102.52

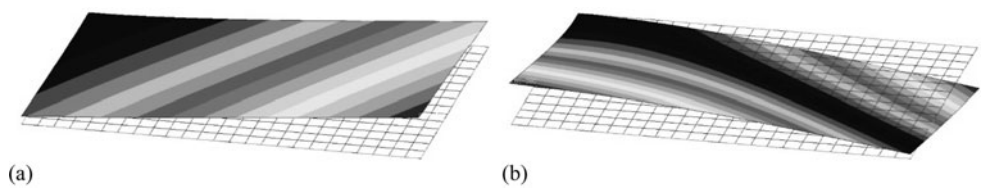

Figure 7. Wing displacement along z-axis regarding a) 1st and b) 2nd structural mode.

5.3 Structural considerations

Given the employed modal approach in dynamic modelling of the structure, the developed equations are valid for all elastic wings with different geometrical shape and features as long as its modal properties, including natural frequencies and mode shapes are available. However, in order to better understand the implementation procedure, a rectangular wing case is investigated in this study.

The considered rectangular wing, Fig. 5, is modelled as cantilever structure. This is because the wing structure is practically being carried by the servomotor connector bar where the EFW is fixed to this connector bar at the junction. As discussed earlier, structural vibrations are obtained around the rigid instantaneous position of the wing and subsequently the inertial position of the wing elements will be computed via Equation (61)

Despite the fact that the extracted relations in Section 3.0 are independent of the structural elements type for FEM analysis, the EFW structure is considered as a Reinforced Rectangular Structure (RRS). The RRS is modelled as a flat plate with dimensions of $1(\text{mm}) \times 300(\text{mm}) \times 500(\text{mm})$, reinforced at the Leading Edge (LE) by a tubular beam of radius 2 mm that adds to the flexural strength about the x^R axis Further, the RRS Aluminium wing has stiffness properties $E = 70$ GPa, $G = 26$ GPa and a mass density of $\rho = 2710$ kg/m^3[48].

The modal properties are determined via FEM for 25×15 elements EFW, where the first 10 modes are taken into account, see Table 1 and Fig. 7. The pertinent values of the Generalised Inertial Moments are computed and tabulated in Table 2.

Generally in a beam-based modelling approach, the elastic axis is a line along which transverse loads only produce bending, while causing no sectional torsion at any spanwise

https://doi.org/10.1017/aer.2018.74 Published online by Cambridge University Press

Table 2
Generalised inertial moment of first 10 structural modes

Mode Number	Value (kg.m)
1	0.1837
2	− 0.0334
3	− 0.0178
4	0.0092
5	0.0064
6	0.0000
7	0.0007
8	0.0027
9	− 0.0011
10	− 0.0032

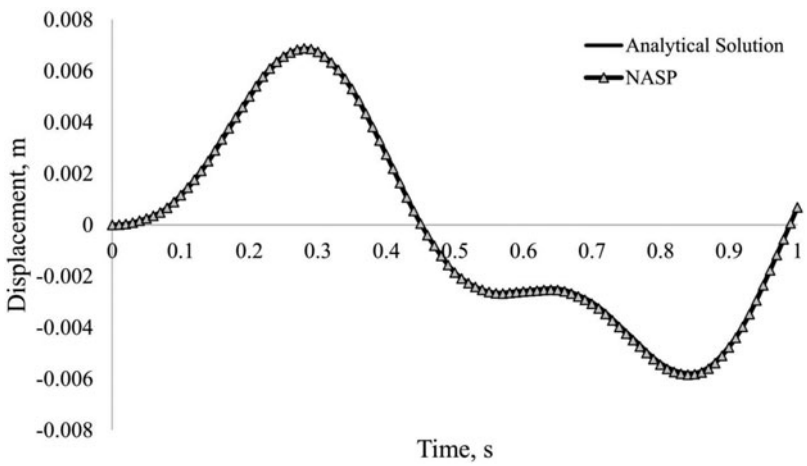

Figure 8. Elastic displacement of point c, from analytical solution versus the transient response in NASP.

station. Considering this concept, it can be deduced from Fig. 7 that both bending as well as torsional wing behaviours occur along an oblique line for the 1st and 2nd structural modes. This oblique line, in fact, shows the position of the elastic axis along the beam length or spanwise direction. This is an important issue often not attended to by researchers[28,30,39] utilizing the beam assumption in which the spanwise displacement of the elastic axis is neglected.

In order to verify the analytical structural solution of the EFW, the commercial Nastran-Patran[49] (NASP) FEM code is utilised whose transient response results for a time-dependent point force, ($f(t) = 0.1\ \sin(2\pi t)$) where $0 < t < 1$ applied to point c (see Fig. 9) of the EFW, is shown in Fig. 8. This figure compares the analytically calculated elastic displacement of point c against the transient response result of NASP. As demonstrated in this figure, both results coincide and thus the proposed analytical solution is accurate and compatible with no-planner-displacement assumption.

https://doi.org/10.1017/aer.2018.74 Published online by Cambridge University Press

Table 3
EFW simulation parameters

Parameters	Value
$t_{\text{Glide}}(\text{sec})$	4.2
$\omega_f(\text{rad}/\text{sec})$	2π
$\gamma_{\max}(\text{deg})$	30
$\gamma_{\text{Glide}}(\text{deg})$	5
ζ_c	0.5
$\omega_c(\text{rad}/\text{sec})$	6
ζ_r	0.07

Table 4
Calculated solution parameters

Mode Number	Value (kg.m)
A_{21}	0.4958
A_{22}	0.6020
ϕ_{22}	0.9675
A_{11}	0.4979
ϕ_{11}	− 1.6628
B_{11}	0.1008
ψ_{11}	1.0472

5.4 Simulation and results

The EFW simulation parameters are listed in Table 3 that has resulted in the solution parameters (using Equations (21) and (32)) given in Table 4.

According to the aforementioned flight scenarios, simulations of the EFW flapping and gliding motion are performed continuously and consecutively. It needs to be mentioned that the number of required modes is problem dependent and it is shown that three modes are sufficient. The effects of taking additional modes numbers for some typical wing nodes shown in Fig. 9 are analytically studied and reported in Figs 10 and 11. As can be seen from Fig. 9, point c is of highest displacement whose value sufficiently converges with only three modes with an accuracy level of better that 0.5 percent as demonstrated in Fig. 11.

Finally, the EFW motion is animated under the influence of the controller dynamics in Fig. 12 at different time steps. Another important observation that emanates out of Fig. 7, indicates that the selected EFW actually undergoes its bending and torsional motion along an oblique elastic axis. This observation demonstrates the complexity and dependency of the EFW dynamic behaviour on its geometric and structural features. Thus, in general, a one-dimensional beam-type model, usually chosen by many researchers[29,39], is improper for dynamic modelling of EFW behaviour unless the variation of elastic axis at each spanwise section is carefully considered. Still, this alone would not guarantee proper accuracy of EFW structural dynamic analysis, as chordwise geometric fluctuations have a great influence on aerodynamic properties of the aerofoil sections and consequently, the whole wing.

https://doi.org/10.1017/aer.2018.74 Published online by Cambridge University Press

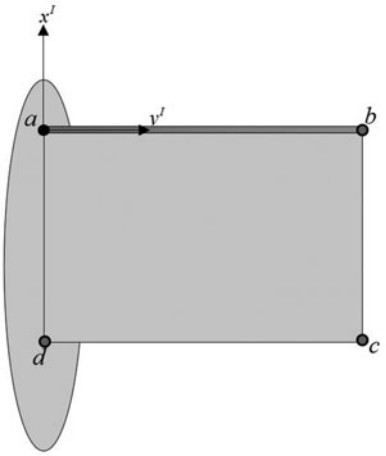

Figure 9. Sample selected nodes.

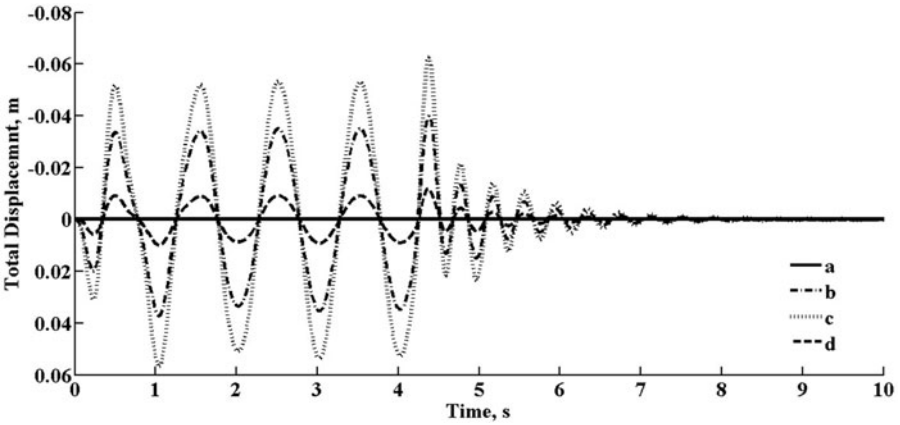

Figure 10. Cycle elastic displacements of the selected sample nodes using 10 modes.

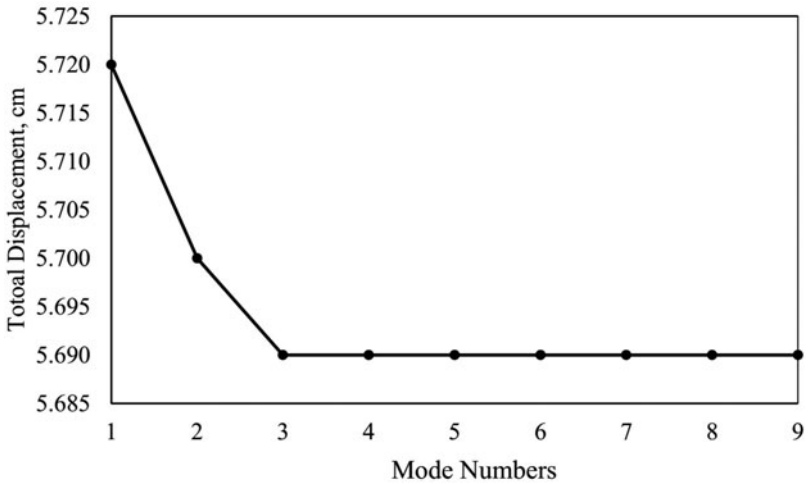

Figure 11. Displacement of point c versus number of modes.

https://doi.org/10.1017/aer.2018.74 Published online by Cambridge University Press

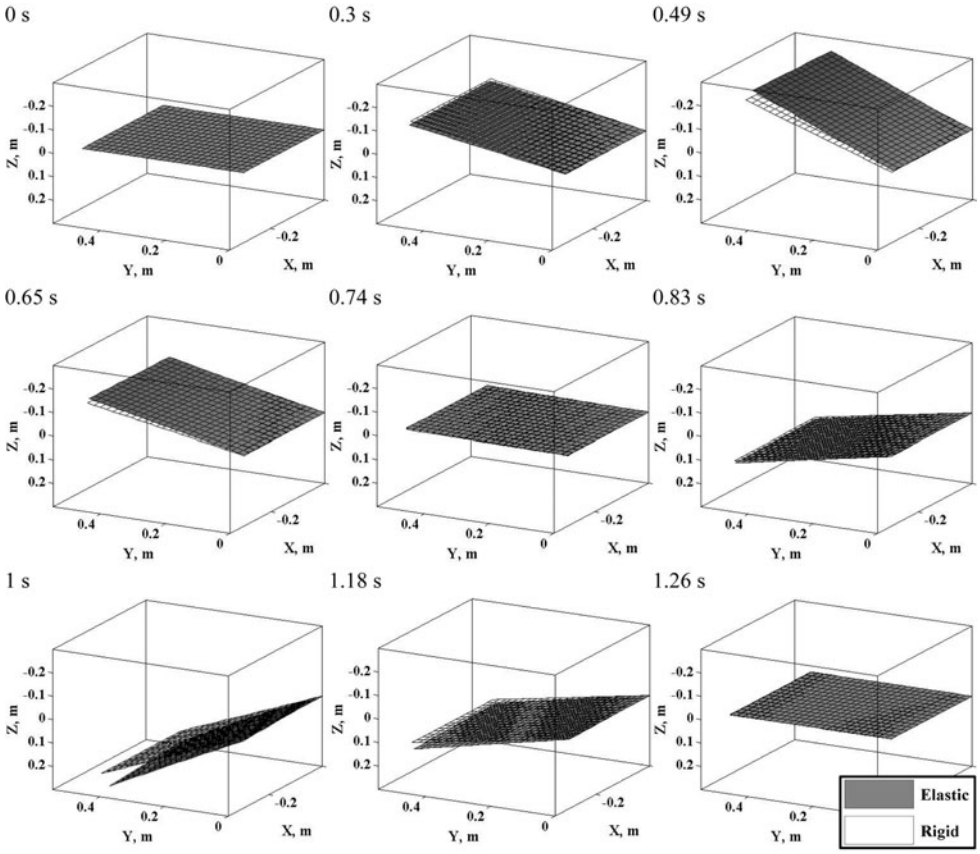

Figure 12. Wing status at first cycle in nine different step times.

6.0 CONCLUSION

An analytical SD solution of an EFW in Transient phase of Flapping and Gliding is presented using a modal approach. The solution is verified under a time-varying loading scenario. Due to the importance of the derivation of an analytical solution for EFW structural in order to conceptually analyse the effect of wing elasticity, the linear-motion range assumption is stipulated.

A common flight scenario of birds flying is simulated in which a wing starts a sinusoidal motion that is subsequently commended to stop at a fixed angular position while the servo dynamics is accounted for. As expected, the results show that the servo dynamics cause a delay as well as a change in the EFW motion amplitude. In the undamped systems, it is realized that resonance occurs if SFFR reach to one. On the other hand, the resonance won't happen in the damped system, but the maximum amplitude occurs when both frequency ratios i.e. SAFR and SFFR equal to one. Elastic sensitivity analyses reveals that one does not need to consider all structural modes, since the amplitudes pertinent to generalised coordinates of high-frequency modes tend towards zero. Another observation using FEM for the mode shapes indicated that both EFW bending and torsion behaviour occur about oblique lines. This is important when using beam assumption to model the elastic behaviour of the EFWs. The study also shows that

https://doi.org/10.1017/aer.2018.74 Published online by Cambridge University Press

one may substitute expensive numerical solution approaches by elegant mathematical based derivations for analysis. Although, because of importance and derivation of analytical results only inertial forces was considered, due to periodic nature of aerodynamic, they can be also taken into account using a similar mathematical methodology using a periodic series forcing such as the Fourier.

ACKNOWLEDGEMENTS

The authors would like to thank Dr. H. Haddadpour of Sharif University of Technology for his helpful suggestions in this study.

REFERENCES

1. SHYY, W., BERG, M. and LJUNGQVIST, D. Flapping and flexible wings for biological and micro air vehicles, *Progress in Aerospace Sciences*, 1999, **35**, pp 455-505.
2. WOOTTON, R.J. Functional morphology of insect wings, *Annual Review of Entomology*, 1992, **37**, pp 113-140.
3. SMITH, M. The effects of flexibility on the aerodynamics of moth wings - Towards the development of flapping-wing technology, 33rd Aerospace Sciences Meeting and Exhibit, 1995.
4. ZHU, Q. Numerical simulation of a flapping foil with chordwise or spanwise flexibility, *AIAA J*, 2007, **45**, pp 2448-2457.
5. MASOUD, H. and ALEXEEV, A. Resonance of flexible flapping wings at low Reynolds number, *Physical Review E*, 2010, **81**, p 056304.
6. NAKATA, T. and LIU, H. Aerodynamic performance of a hovering hawkmoth with flexible wings: a computational approach, *Proceedings: Biological Sciences*, 2012, **279**, pp 722-731.
7. WENQING, Y., LIGUANG, W., DONG, X. and BIFENG, S. Aerodynamic performance of micro flexible flapping wing by numerical simulation, *Procedia Engineering*, 2015, **99**, pp 1506-1513.
8. OLIVIER, M. and DUMAS, G. Effects of mass and chordwise flexibility on 2D self-propelled flapping wings, *J Fluids and Structures*, 2016, **64**, 46-66.
9. OLIVIER, M. and DUMAS, G. A parametric investigation of the propulsion of 2D chordwise-flexible flapping wings at low Reynolds number using numerical simulations, *J Fluids and Structures*, 2016, **63**, pp 210-237.
10. TAY, W.B. Symmetrical and non-symmetrical 3D wing deformation of flapping micro aerial vehicles, *Aerospace Science and Technology*, 2016, **55**, pp 242-251.
11. COMBES, S.A. and DANIEL, T.L. Into thin air: contributions of aerodynamic and inertial-elastic forces to wing bending in the hawkmoth Manduca sexta, *J Experimental Biology*, 2003, **206**, pp 2999-3006.
12. SHYY, W., IFJU, P. and VIIERU, D. Membrane wing-based micro air vehicles, *Applied Mechanics Reviews*, 2005, **58**, pp 283-301.
13. HEATHCOTE, S., WANG, Z. and GURSUL, I. Effect of spanwise flexibility on flapping wing propulsion. *J Fluids and Structures*, 2008, **24**, pp 183-199.
14. HU, H., KUMAR, A.G., ABATE, G. and ALBERTANI, R. An experimental study of flexible membrane wings in flapping flight, 47th AIAA Aerospace Sciences Meeting Including the New Horizons Forum and Aerospace Exposition, AIAA, Orlando, Florida, US, 2009.
15. LUA, K., LAI, K., LIM, T. and YEO, K. On the aerodynamic characteristics of hovering rigid and flexible hawkmoth-like wings. *Experiments in fluids*, 2010; **49**, 1263-1291.
16. MAZAHERI, K. and EBRAHIMI, A. Experimental study on interaction of aerodynamics with flexible wings of flapping vehicles in hovering and cruise flight, *Archive of Applied Mechanics*, 2010, **80**, pp 1255-1269.
17. MOUNTCASTLE, A.M. and DANIEL, T.L. Aerodynamic and functional consequences of wing compliance, *Animal Locomotion*, 2010, pp 311-320.
18. WU, P., IFJU, P. and STANFORD, B. Flapping wing structural deformation and thrust correlation study with flexible membrane wings, *AIAA J,* 2010, **48**, pp 2111-2122.

https://doi.org/10.1017/aer.2018.74 Published online by Cambridge University Press

19. ZHAO, L., HUANG, Q., DENG, X. and SANE, S.P. Aerodynamic effects of flexibility in flapping wings, *J Royal Society Interface*, 2010, **7**, pp 485-497.
20. LARIJANI, R.F. and DELAURIER, J.D. A non-linear aeroelastic model for the study of flapping wing flight, *Progress in Astronautics and Aeronautics*, 2001, **195**, pp 399-428.
21. SINGH, B. and CHOPRA, I. An aeroelastic analysis for the design of insect-based flapping wings, 48th AIAA/ASME/ASCE/AHS/ASC Structures, Structural Dynamics, and Materials Conference, 2007.
22. GOGULAPATI, A., FRIEDMANN, P. and SHYY, W. Non-linear aeroelastic effects in flapping wing micro air vehicles, 49th AIAA/ASME/ASCE/AHS/ASC Structures, Structural Dynamics, and Materials Conference, Schaumburg, Illinois, US, 2008.
23. BANERJEE, S.P. and PATIL, M. Aeroelastic analysis of membrane wings, 49th AIAA/ASME/ASCE/AHS/ASC Structures, Structural Dynamics, and Materials Conference, University Libraries, Virginia Polytechnic Institute and State University, Schaumburg, Illinois, US, 2008.
24. KIM, D.-K. and HAN, H. A dynamic model of a flexible flapping wing for fluid-structure interaction analysis, 15th International Congress on Sound and Vibration, 2008.
25. CHIMAKURTHI, S.K., TANG, J., PALACIOS, R.S., CESNIK, C.E. and SHYY, W. Computational aeroelasticity framework for analyzing flapping wing micro air vehicles, *AIAA J*, 2009, **47**, pp 1865-1878.
26. KHURI, A.I. and MUKHOPADHYAY, S. Response surface methodology, *Wiley Interdisciplinary Reviews: Computational Statistics*, 2010, **2**, pp 128-149.
27. AONO, H., KANG, C., CESNIK, C.E. and SHYY, W. A numerical framework for isotropic and anisotropic flexible flapping wing aerodynamics and aeroelasticity, 28th AIAA Applied Aerodynamics Conference, Chicago, Illinois, US, 2010.
28. SU, W. and CESNIK, C. Nonlinear aeroelastic simulations of a flapping wing micro air vehicle using two unsteady aerodynamic formulations, 51st AIAA/ASME/ASCE/AHS/ASC Structures, Structural Dynamics, and Materials Conference, Orlando, Florida, US, 2010.
29. POURTAKDOUST, S.H. and KARIMAIN ALIABADI, S. Evaluation of flapping wing propulsion based on a new experimentally validated aeroelastic model, *Scientia Iranica*, 2012, **19**, pp 472-482.
30. DE ROSIS, A., FALCUCCI, G., UBERTINI, S. and UBERTINI, F. Aeroelastic study of flexible flapping wings by a coupled lattice Boltzmann-finite element approach with immersed boundary method, *J Fluids and Structures*, 2014, **49**, pp 516-33.
31. LAKSHMINARAYAN, V.K. and FARHAT, C. Nonlinear aeroelastic analysis of highly flexible flapping wings using an ALE formulation of embedded boundary method, AIAA Science and Technology Forum and Exposition, National Harbor, Maryland, US, 2014.
32. NOGAR, S., GOGULAPATI, A., MCNAMARA, J.J. and SERRANI, A. Approximate dynamics modeling of flexible flapping wing MAVs with application to control, AIAA Atmospheric Flight Mechanics Conference, National Harbor, Maryland, US, 2014.
33. HA, N.S., TRUONG, Q.T., PHAN, H.V., GOO, N.S. and PARK, H.C. Structural characteristics of allomyrina dichotoma beetle's hind wings for flapping wing micro air vehicle, *J Bionic Engineering*, 2014, **11**, pp 226-235.
34. DJOJODIHARDJO, H. Analysis and computational study of the aerodynamics, aeroelasticity and flight dynamics of flapping wing ornithopter using linear approximation, 54th AIAA Aerospace Sciences Meeting, San Diego, California, US, 2016.
35. DANIEL, T.L. and COMBES, S.A. Flexible wings and fins: bending by inertial or fluid-dynamic forces?, *Integr Comp Biol.*, 2002, **42**, pp 1044-1049.
36. BARUT, A., DAS, M. and MADENCI, E. Nonlinear deformations of flapping wings on a micro air vehicle, Newport, Rhode Island, US, 2006.
37. WILSON, N. and WERELEY, N. Experimental investigation of flapping wing performance in hover, 48th AIAA/ASME/ASCE/AHS/ASC Structures, Structural Dynamics, and Materials Conference, 2007, American Institute of Aeronautics and Astronautics.
38. YEO, D., ATKINS, E.M., BERNAL, L.P. and SHYY, W. Experimental characterization of lift on a rigid flapping wing, *J Aircraft*, 2013, **50**, 1806-1821.
39. ISOGAI, K. and HARINO, Y. Optimum aeroelastic design of a flapping wing, *J Aircraft*, 2007, **44**, pp 2040-2048.
40. PLATUS, D. Aeroelastic stability of slender, spinning missiles, *J Guidance, Control, and Dynamics*, 1992, **15**, pp 144-151.

https://doi.org/10.1017/aer.2018.74 Published online by Cambridge University Press

41. POURTAKDOUST, S. and ASSADIAN, N. Investigation of thrust effect on the vibrational characteristics of flexible guided missiles, *J Sound and Vibration*, 2004, **272**, pp 287-299.
42. MEIROVITCH, L. and TUZCU, I. *Integrated approach to the dynamics and control of maneuvering flexible aircraft,* 200,3 National Aeronautics and Space Administration, Langley Research Center.
43. LI, Y., NAHON, M. and SHARF, I. Dynamics modeling and simulation of flexible airships, *AIAA J*, 2009, **47**, pp 592-605.
44. HOLLKAMP, J.J. and GORDON, R.W. Reduced-order models for nonlinear response prediction: Implicit condensation and expansion, *J Sound and Vibration*, 2008, **318**, pp 1139-1153.
45. RIZZI, S.A. and MURAVYOV, A.A. Equivalent linearization analysis of geometrically nonlinear random vibrations using commercial finite element codes, NASA Technical Paper TP-2002-211761, 2002.
46. MCEWAN, M.I. A Combined Modal/Finite Element Technique for the Non-linear Dynamic Simulation of Aerospace Structures, PhD thesis, 2001, University of Manchester, England.
47. OGATA, K. *Modern Control Engineering*, Prentice Hall, 2010, Upper Saddle River, New Jersey, US.
48. BEER, F.P. E. JR, RUSSELL, JOHNSTON, DEWOLF, JOHN T. and MAZUREK, DAVID F. *Mechanics of Materials*, 2011, McGraw-Hill, New York, New York, US.
49. MSC. *Nastran 2010 User's Manual*: MSC.Software Corporation, 2010.

https://doi.org/10.1017/aer.2018.74 Published online by Cambridge University Press